https://doi.org/10.5194/essd-2022-286
Preprint. Discussion started: 26 September 2022

Open Access Earth System Science Data Discussions

High-resolution maps of above- and belowground woody biomass in China from 2003 to 2020

Yongzhe Chen[1,2], Xiaoming Feng[1,2], Bojie Fu[1,2], Haozhi Ma[3], Constantin M. Zohner[3], Thomas W. Crowther[3], Yuanyuan Huang[4,5], Xutong Wu[6], Fangli Wei[1]

[1] State Key Laboratory of Urban and Regional Ecology, Research Center for Eco-Environmental Sciences, Chinese Academy of Sciences, Beijing, PR China.

[2] College of Resources and Environment, University of Chinese Academy of Sciences, Beijing, PR China.

[3] Institute of Integrative Biology, ETH Zurich (Swiss Federal Institute of Technology), Zurich, Switzerland.

[4] Laboratoire des Sciences du Climat et de l'Environnement, LSCE/IPSL, CEA-CNRS-UVSQ, Université Paris-Saclay, Gif-sur-Yvette, France

[5] Commonwealth Scientific and Industrial Research Organisation, Aspendale, Victoria, Australia

[6] State Key Laboratory of Earth Surface Processes and Resource Ecology, Faculty of Geographical Science, Beijing Normal University, Beijing, PR China.

Correspondence to: Xiaoming Feng (fengxm@rcees.ac.cn)

Abstract. To quantify the ecological consequences of recent nation-wide restoration efforts in China, spatially-explicit information on woody biomass changes over the 21st century is critical. However, long-term biomass tracking at the national scale remains challenging as it requires continuous and high-resolution monitoring. Here, we mapped above- and belowground biomass (AGB and BGB) for woody vegetation in China between 2003 and 2020 at ~1 km spatial resolution by integrating multiple types of remote sensing observations with intensive field plot measurements through machine learning and mixed-pixel decomposition methods. On average, 11.0 ± 0.7 and 2.8 ± 0.2 PgC are stored in above- and belowground live woody biomass in China. Over the last 18 years, the total woody biomass carbon in China has increased at a rate of 163.8 TgC yr^{-1} (0.5% yr^{-1}). The most pronounced biomass gains occurred in central to southern China, including the southern Loess Plateau, Qinling Mountains, southwest karst and southeast forests. The combined use of low-frequency (L-band, etc.) microwaves and laser remote sensing data provides a powerful tool to minimize under- or overestimation of biomass variation in space and time. Future research is needed to explore the drivers of the observed woody biomass trends, and to evaluate the degree to which biomass gains will translate into biodiverse, healthy ecosystems and thus are sustainable.

https://doi.org/10.5194/essd-2022-286
Preprint. Discussion started: 26 September 2022

1 Introduction

Woody (forest and shrubland) biomass contributes to over 90% of global vegetation biomass (Ma et al., 2021). As a net outcome of carbon gains from photosynthesis and carbon losses from respiration, mortality and disturbances, woody biomass is a critical indicator of ecosystem function and services, such as carbon sequestration, wood production and resource allocation (Kumar and Mutanga, 2017). Accurate biomass monitoring over space and time is thus essential for assessing ecosystem management strategies and mitigation policies (Kumar and Mutanga, 2017).

In recent decades, remote sensing tools have been integral in the efforts to map aboveground biomass (AGB). By combining satellite imagery (e.g., MODIS) and airborne LiDAR signals, forest cover and canopy height can be mapped across large spatial scales (Hu et al., 2016; Saatchi et al., 2011; Su et al., 2016; Tong et al., 2020; Xu et al., 2021). Apart from imageries and LiDAR signals, microwaves can provide more detailed insights into sub-canopy forest structure and AGB due to their ability to penetrate the canopy. Active microwave techniques, i.e., Synthetic Aperture Radar (SAR) backscatters, facilitate high-resolution (e.g., 100 m) AGB mapping, but the temporal coverage is limited (Cartus et al., 2012; Bouvet et al., 2018). Conversely, vegetation optical depth (VOD) retrieved from multiple passive microwave sensors can be used to produce long-term continuous AGB maps (Frappart et al., 2020; Liu et al., 2011; Liu et al., 2015), yet at a coarse spatial resolution (e.g., 0.25°). Because optical, LiDAR and microwave (both active and passive) remote sensing techniques all have their advantages and limitations, combining these techniques and complementing them with direct ground measurements is integral to reducing the uncertainty in long-term continuous and high-resolution AGB mapping.

Another source of uncertainty in vegetation biomass stocks is the extent of biomass that is stored belowground as roots. While AGB mapping is facilitated by the suite of emerging remote sensing techniques, investigating the spatiotemporal variation in belowground biomass (BGB) remains challenging despite the large contribution of root biomass to total carbon storage (Huang et al., 2021; Ma et al., 2021). To map BGB, the commonly-used approach is to combine aboveground biomass information with vegetation type-specific ratios of BGB to AGB (i.e., root-shoot ratio, or RSR) (Xu et al., 2021; Saatchi et al., 2011). Because field studies indicate a near-linear relationship between log-transformed BGB and AGB

https://doi.org/10.5194/essd-2022-286
Preprint. Discussion started: 26 September 2022

(Enquist Brian and Niklas Karl, 2002), BGB variations at large scales have often been approximated using this relationship (Spawn et al., 2020). To capture the complex relationship between BGB and biotic or abiotic variables (e.g., stand age, heat and water availability), machine learning algorithms have been applied to map BGB (Huang et al., 2021) and root-mass fractions (Ma et al., 2021) globally. In mixed pixels with multiple plant functional types, BGB mapping relying on satellite-based AGB and plot-based models is expected to be less accurate. In addition, the existing woody plots are unevenly distributed across the world, with limited plots in developing countries, leading to large uncertainties in BGB estimation within those regions (Huang et al., 2021).

China has been implementing national-scale afforestation and reforestation programs since the late 1990s (Lu et al., 2018), promoting vegetation cover and carbon storage in the Loess Plateau and the southwest karst regions, etc. (Chen et al., 2019a; Niu et al., 2019; Tong et al., 2018). A spatial understanding of woody biomass trends can help evaluate the efficiency of ecological restoration programs. High quality, high resolution and long-term continuous woody biomass monitoring in China has remained challenging, due to difficulties in integrating different remote sensing techniques with ground-sourced measurements (Zhang et al., 2019; Huang et al., 2019).

In this study, we integrate different remote sensing tools (optical, active/passive microwave and LiDAR) with large quantities of plot measurements through random forest approach to produce high-resolution (1 km) above- and belowground woody biomass maps in China during 2003–2020. This dataset could provide new insights into the spatial hotspots of woody biomass and its interannual changes over the past two decades.

2 Materials and methods

To map above- and belowground woody biomass in China during 2003–2020, we 1) integrated state-of-the-art satellite-derived forest AGB and canopy height information with ground-sourced plot data; 2) developed an improved vegetation water content (VWC) dataset covering 2003–2020 based on the intercalibration of vegetation optical depth retrieved from various microwave sensors; 3) combined multiple sources of remote sensing and in-situ observations simultaneously

https://doi.org/10.5194/essd-2022-286
Preprint. Discussion started: 26 September 2022

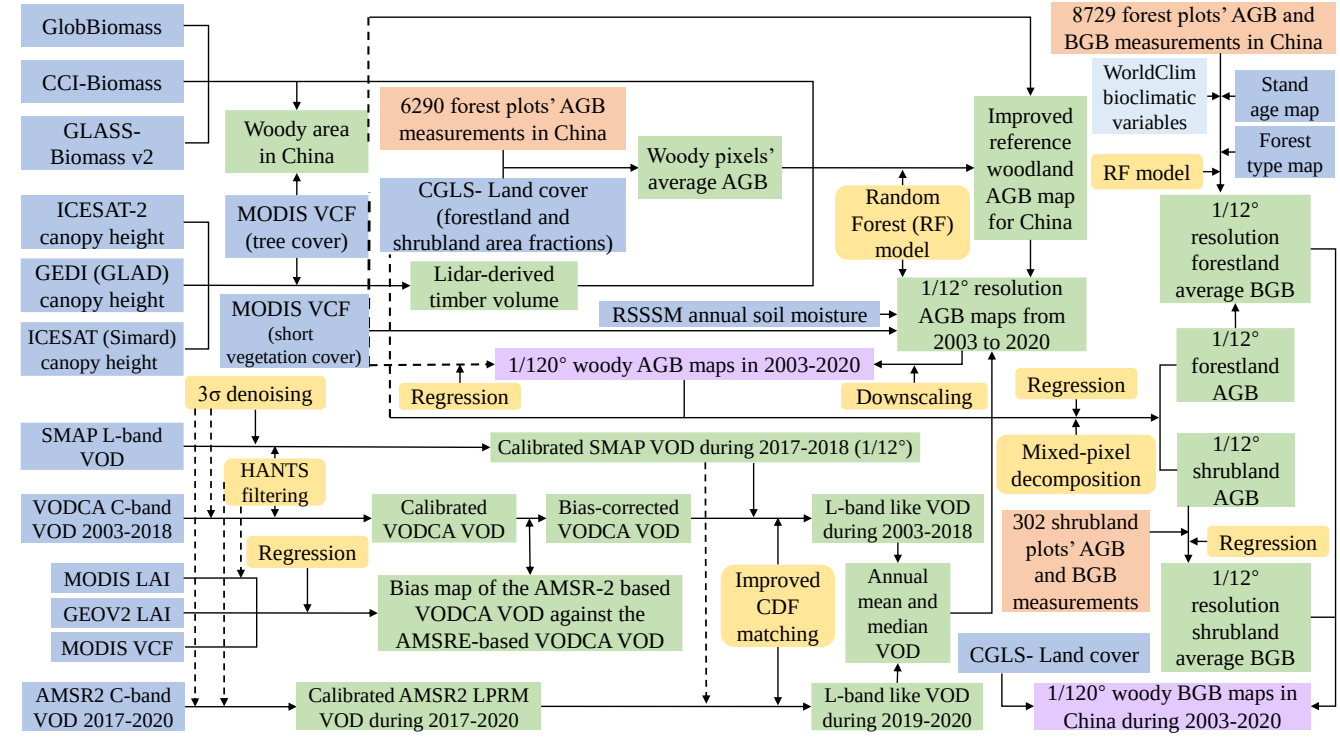

Figure 1: Workflow of woody AGB and BGB monitoring in China during 2003–2020. The blue rectangles are remote sensing-based data inputs (data sources are listed in Text S3); orange rectangles are plot-level measurements; yellow rectangles represent the key methods; green rectangles are the intermediate results; while the purple rectangles represent the final outputs of this study. 'GlobBiomass', 'CCI', etc. are data products' names; 'CDF' = 'cumulative distribution function'; 'HANTS' = 'harmonic analysis of time series'; 'VCF' = vegetation continuous fields. Locations of the collected forest plots are shown in Figure S1a.

2.1 An improved benchmark map of aboveground biomass (AGB) in China

We used the three latest high-quality global-scale AGB datasets (GlobBiomass, CCI-Biomass and GLASS-Biomass v2) to derive our benchmark map. Using SAR, LiDAR and optical images, the first global high-resolution (100 m) forest AGB dataset for the year 2018, GlobBiomass, was published through the European Space Agency (ESA)'s Data User Element

https://doi.org/10.5194/essd-2022-286
Preprint. Discussion started: 26 September 2022

(DUE) project (Santoro et al., 2021). The relative root mean square error (RMSE) was below 30%, although biomass tends to be underestimated in dense forests (Mialon et al., 2020). Subsequently, ESA's Climate Change Initiative (CCI) published a global AGB map for all vegetation in 2017 using a slightly different algorithm, followed by AGB maps for 2010, 2018 and 2019 (Santoro and Cartus, 2019, 2021). Datasets derived from different methods have their advantages in different regions. By referring to adequate in-situ data, we may combine the advantages of different datasets. Accordingly, integration of several high-quality AGB maps has become popular. The Global Land Surface Satellite (GLASS) AGB v2 was developed by fusing the AGB maps in (Hu et al., 2016), (Su et al., 2016) and (Thurner et al., 2014), etc., through the linear combination method. GLASS-Biomass v2 roughly represents the AGB status in the year 2000, the median period of the collected woody plots' data (Zhang and Liang, 2020).

We aggregated the GlobBiomass and CCI-Biomass maps from 1/1125° resolution to 1/120° (approximately 1 km) and resampled the GLASS-Biomass product from 0.01° to 1/120°. Because the biomass of herbaceous vegetation was not included in GlobBiomass and GLASS-Biomass datasets due to the high uncertainty, the study area in this study was determined as all the 1/120° pixels (note: the 1/120° resolution is referred to as a pixel hereinafter) for which AGB data are available from each of these three woody biomass datasets.

In September 2018, ICESat-2 provided an Advanced Topographic Laser Altimeter System (ATLAS) that provides more accurate and denser measurements of canopy height than GLAS (Markus et al., 2017). ICESAT-2 data have been applied in canopy height estimation at large scales (Liu et al., 2022). This study selected the ATL08 land and vegetation V004 product, and the 98% height retrievals of all canopy photons in each 100 m segment can best represent the mean top canopy height (Neuenschwander et al., 2020). All ATLAS records acquired in China's woody areas during 2018~2020 were incorporated. ATLAS has three strong and three weak beams. According to previous studies, the canopy heights retrieved using strong beams are generally more accurate than those retrieved by weak beams (Neuenschwander et al., 2020). Hence, in each 1/120° resolution pixel, we counted the numbers of valid strong beam and weak beam observations within the pixel during 2018~2020. If the number of strong beam records exceeded 5, then only those higher quality data were used. Otherwise, if there were at least 5 valid observations, but the number of strong beam retrievals was not enough, all data in the pixel were

https://doi.org/10.5194/essd-2022-286
Preprint. Discussion started: 26 September 2022

incorporated. Afterwards, we adopted the median absolute deviation (MAD) method to detect and eliminate outliers (Leys et al., 2013). For the remaining reliable canopy height retrievals in each pixel, we took the average weighted by the corresponding canopy cover fractions. Here, the top canopy cover fraction was estimated as the ratio of canopy photons to the number of all photons in the 100 m segment. By following the above steps, we mapped forest height over China using ATLAS data. Because gaps remain between the tracks of ICESAT-2, although ATLAS's six beams enable a larger spatial coverage than other LiDAR instruments, the derived forest height map provides values in only 42% of all woody pixels in China. Because of the potentially bad LiDAR estimates, the highest 2.5% extreme values were further excluded.

Another new LiDAR instrument is NASA's Global Ecosystem Dynamics Investigation (GEDI). It is optimized for global canopy height estimation, and has been collecting data in China since April 2019 (Dubayah et al., 2020). However, the orbital gaps of GEDI are much larger than that of ICESAT-2, resulting in a quite limited spatial coverage by direct observation. Therefore, this study adopted the Global Forest Canopy Height 2019 dataset provided by the Global Land Analysis and Discover (GLAD). GLAD's canopy height was mapped by integrating the GEDI's forest structure measurements globally with Landsat maps through machine learning (Potapov et al., 2020). The original 30 m resolution data were averaged to 1/120°. GEDI does not collect data in north of 51.6°N (Dubayah et al., 2020), but the highest latitude of China is about 53.56°N. Therefore, we used an alternative global gridded forest height map that was developed earlier through machine learning, yet based on the ICESAT GLAS retrievals (Simard et al., 2011).

Because AGB is more related to the forest volume rather than just the canopy height, we further multiplied the three different LiDAR-based canopy height maps with the percent of tree cover (hereinafter TC) acquired from MOD44B v006- dataset. The products of multiplications are hereinafter ATLAS-derived volume, GEDI-derived volume and GLAS-derived volume. None of these LiDAR-based timber volumes cover all woodland pixels in China. Specifically, without spatial interpolation using optical remote sensing, the ATLAS-derived volume inherited the orbital gaps of ICESAT-2, although the quality is expected higher than that of the other two machine learning-derived canopy heights and volumes. Thus, we designed three random forests for AGB estimation. Each of these three random forests (RFs) have four input predictors. GlobBiomass, CCI-Biomass and GLASS-Biomass v2, are incorporated as the predictors of each RF, while the use of which LiDAR-derived

https://doi.org/10.5194/essd-2022-286
Preprint. Discussion started: 26 September 2022

volume as the 4th input predictor makes the difference among the three RFs. Moreover, to reduce uncertainties in LiDAR-derived timber volumes, the pixels with tree cover below 5% are classified as nonwoody areas and excluded.

The training target should be a large number of high-quality 1/120° pixel-scale AGB data in China. This study collated forest or shrubland plots' AGB calculated using allometric equations or clear-cutting methods from various published papers, including (Luo, 1996), (Luo et al., 2014), (Guo and Ren, 2014), (Peng et al., 2016), (Wang et al., 2014), (Guo et al., 2021), (Yang et al., 2017), (Liu et al., 2020) and (Nie et al., 2016). In addition to AGB, we recorded the BGB, stand age, vegetation species or type and location information. The spatial distributions of all these woody plots are shown in Figure S1a. Some records were measured in 1990~2000, whereas others were acquired during 2000~2010. Although the nominal periods of plot measurements are different from those of the remote sensing-based predictor biomass maps (i.e., 2017~2020), it is supposed that the spatial pattern of woody biomass at 1 km resolution would not change much from around 2000 to 2017~2020, so the time lag problem could be ignored. However, because plots smaller than 0.05 ha are not comparable to satellite observations (Su et al., 2016), 10 m×10 m plots (Guo and Ren, 2014) were not included as the training target here, but were applicable in determining the biomass allocation rule later in section 2.5. Moreover, the understory shrub AGB was excluded, since SAR and LiDAR can observe only the canopy. The extreme values (the highest and lowest 1%) were excluded as well. These filters resulted in 6290 woody plots remaining. Because the plots are mainly located in woodlands, yet the corresponding pixel usually contains cropland, urban, waters or bare ground, whose AGB are much lower than those in the plots, we converted the plot-level AGB into the pixel-scale AGB by multiplying the area fraction of forestland in the pixel, as long as the forestland area fraction exceeds 20% and is larger than the shrubland area fraction. Here, land cover type comes from the Copernicus Global Land Service: Land Cover 100m (CGLS-LC)- epoch 2017: v3.0.1 data (Buchhorn et al., 2020). It includes not only discrete land cover classification but also the fractions of forestland, shrubland, grassland and cropland at 100 m resolution. We aggregated these high-resolution land cover fractions to 1/120° to reduce the uncertainties. It should be noted that VCF data cannot be applied here because they indicate the fractions of pure tree cover and short vegetation cover, yet a forestland contains bare ground or herbs among trees.

The RF model trainings were conducted in MATLAB R2021a software. After the RF trainings, three sets of simulations were

https://doi.org/10.5194/essd-2022-286
Preprint. Discussion started: 26 September 2022

performed using the corresponding RF model in woody pixels where all four predictors (three existing AGB products and one LiDAR-derived volume) have valid data. In addition, we performed ten-fold cross-validation to assess the performance of each RF model, and took the averages of ten times of simulations. Finally, we combined the three sets of simulations by averaging that is weighted by the mean R^2 of the corresponding RF model. Using above methods, we produced a spatially-continuous 1/120° benchmark AGB map for China. Because most of these measurements (i.e., training targets) refer to the vegetation biomass status in around 2000, we expect our AGB map to represent the AGB in around 2000 (although the predictor AGB maps are for 2017~2020, they are just used as the indicators of the spatial variability rather than the absolute values). Therefore, our improved benchmark AGB map is hereinafter named 'AGBbenchmark-2000s'.

In addition, we exported the importance of each predictor variable in the RF models. For any variable, the measure is the increase in prediction error if the values of that variable are permuted across the out-of-bag observations. This measure is computed for every tree, then averaged over the entire ensemble and divided by the standard deviation of the entire ensemble.

2.2 An improved vegetation optical depth dataset covering 2003–2020

To derive a long time series of AGB, long-term continuous microwave VOD (i.e., vegetation opacity) data is useful (Jackson and Schmugge, 1991; O'neill et al., 2021). Through cumulative distribution function (CDF) matching among different VOD products, the vegetation optical depth climate archive (VODCA) was developed(Moesinger et al., 2020). The 'C-band' product which was retrieved using several C-band microwave sensors including AMSR-E, WindSat and AMSR2 and covers 2003~2018, is a better indicator of the whole woody plants' biomass than those retrieved using higher frequency microwave bands (i.e., X-band and Ku-band). However, compared to the VOD retrieved from L-band sensors such as SMOS (Wigneron et al., 2021) and SMAP (Konings et al., 2017), C-band VODs are still less sensitive to the biomass of trunks and branches, which contribute most to the AGB (Li et al., 2021). Therefore, C-band VODs usually have high-frequency variations due to the strong variation in leaf water content per biomass under rainfall or drought events (Li et al., 2021). In addition, VODCA's C-band product is not perfectly continuous. Because the AMSR2 sensor does not share any temporal overlap with AMSR-E, the rescaling of AMSR2 data towards AMSR-E was based on the assumption that VOD remained stable over 2010~2013, i.e.,

https://doi.org/10.5194/essd-2022-286
Preprint. Discussion started: 26 September 2022

the last and first two years of both sensors. For China where land use cover changes were prevalent, this assumption may lead to a bias of AMSR2-based VODCA data during 2013~2018 compared to the values in this period if the retrievals from AMSR-E were available. Theoretically, this bias is spatially variable, and is positively correlated with local VOD changes from 2010 to 2013. Thus, to develop an improved VOD dataset covering 2003–2020 for China, we focused on 1) filtering out the high-frequency fluctuations in VODCA's product and other C-band VOD products; 2) mapping and correcting the bias of AMSR2-based VODCA data during 2013~2018 compared to the AMSR-E-based VODCA VOD; 3) rescaling the C-band VODs against L-band VOD data to make their spatial patterns more correlated with that of woody plants' AGB; 4) extending the VODCA dataset to 2020 by using AMSR2 observations. Details are as follows.

Due to a very high level of radio frequency interference (RFI), SMOS data are noisy and even missing in China, especially in eastern China (Wigneron et al., 2021), making it inapplicable to this study despite its longer time series than SMAP. SMAP observations have been available since April 2015, so this study utilized the data from 2016 to 2020. The dual channel algorithm (DCA) derived-VOD data included in the SMAP Enhanced L3 v5 product (O'neill et al., 2021) were resampled from 9 km resolution to 1/12°. For each 1/12° grid cell (note: 1/12° resolution is hereinafter called a grid cell) where at least 609 (i.e., 1/3 of 1827 daily maps in 5 years) valid VOD retrievals are available, we first filtered the abnormal values using '3σ denoising' (Chen et al., 2021). Second, we virtually filled in the data in 2015 and 2021 by using those in 2016 and 2020. Subsequently, the no-data values resulting from orbital gaps or frozen states were filled by linear interpolation, while the outputs during 2016~2020 were supposedly valid. Moreover, we also determined the average annual number of VOD peaks for each grid after setting the thresholds of minimum distance between two peaks, peak height and dominance of peaks to reasonable values. Specifically, for grid cells where woody plants exist yet without VOD data, the values were filled by sequentially searching and averaging nearby valid values (Chen et al., 2019b). For VODCA's C-band VOD during 2003~2018, after filtering out the abnormal values and virtually filling the data in 2002 and 2019, we performed the Harmonic Analysis of Time Series (HANTS) filtering(Menenti et al., 1993; Roerink et al., 2000). Either high or low outliers were excluded, while the number of frequencies to be considered above zero frequency in the Fourier function was set to the product of the mean annual peak number detected by SMAP VOD and the number of years.

https://doi.org/10.5194/essd-2022-286
Preprint. Discussion started: 26 September 2022

We then mapped the bias of AMSR2-based VODCA's VOD compared to the AMSR-E based VODCA VOD data in 2003~2011. Because annual VOD is closely related to the leaf area index (LAI), and is clearly affected by percent tree cover and percent nontree vegetation (i.e., crops, grass and shrubs) cover, we performed a multiple linear regression between annual medians of adjusted VODCA VOD data during the period of 2003~2011 and annual LAI values as well as VCF retrievals. This study employed LAI from two sources. First, we processed the potential cloud-affected values within the MODIS LAI product (MCD15A2H v006) by masking the values flagged by clouds and then performing HANTS filtering, with low outliers excluded and the number of frequencies set to 3 times the number of years. Second, for the LAI developed by the ESA- Copernicus Global Land Service (GEOV2 LAI) (Baret et al., 2013; Verger et al., 2014), we harmonized the retrievals from the SPOT-VGT sensor during 2003~2013 and those from the PROBA-V sensor after 2014 using CDF matching with MODIS data applied as the reference (Cammalleri et al., 2019). The MODIS LAI, VCF and GEOV2 LAI were all averaged from their original spatial resolutions (250m~1km) to 0.25° to match the resolution of VODCA. As shown in Figure S2a~b, after the regression, the R^2 values of 90% grids exceeded 0.3, and the grid-specific regression coefficients were exported. Therefore, the mean bias of AMSR2-based VODCA data during 2013~2018 compared to that before 2012 could be estimated as the difference between the mean annual VOD calculated based on the above regression coefficients as well as LAI and VCF data during 2013~2018 and the mean value of the adjusted VODCA's medians over that period. This bias was positive in most areas of China, especially afforested areas, such as northern Beijing (Figure S2c~d). Accordingly, by adding this bias to the VODCA VOD data after 2013, we improved its temporal continuity.

Using SMAP's 1/12° VOD data during 2017~2018 as the reference, we calibrated the spatial pattern of the adjusted VODCA VOD by rescaling. Notably, we revised the CDF matching algorithm (Moesinger et al., 2020). For either the lowest or the highest 10% of the time series, a linear fitting model was designed and applied, to eliminate abnormally low or high values. Finally, to ensure a temporally-consistent VOD time series from 2003 to 2020, for 2019 and 2020, we adopted the AMSR2 C-band VOD and converted it into L-band-like VOD by referring to SMAP data. Here, we chose the AMSR2/GCOM-W1 surface soil moisture (LPRM) L3 1 day 10 km x 10 km descending V001 dataset, and resampled it to 1/12° resolution. Upon noticing sharp changes in AMSR2 VOD at the beginning of 2016 in many grid cells in China, this study selected the records

https://doi.org/10.5194/essd-2022-286
Preprint. Discussion started: 26 September 2022

from only 2017~2020, which were calibrated and rescaled later through improved CDF matching by referring to the SMAP's VOD during 2017~2018.

Using the temporally-continuous and spatially L-band-like VOD dataset from 2003 to 2020, we calculated both annual mean and median VOD values as two robust indicators of annual AGB.

2.3 High-resolution woodland AGB mapping in China from 2003 to 2020

We performed two steps to map woodland AGB in China during 2003–2020. For the first step, AGBbenchmark-2000s and VCF data in 2003 were all resampled to 1/12° resolution, the same as VOD data. Specifically, for grid cells in which less than 50% of pixels were without valid AGBbenchmark-2000s values due to limited forest cover, resampling was not performed. Because VOD is influenced by the soil water availability, we built a random forest in which the predictors include: mean and median VOD values, VCF data (i.e., TC and all vegetation cover, hereinafter denoted as VC) and the mean surface soil moisture (SSM) in 2003. Here, SSM was derived from a long-term remote sensing-based surface soil moisture (RSSSM) developed in our previous study (Chen et al., 2021). The training target is the resampled AGBbenchmark-2000s. More than 80000 grids all across China were available for the training of this RF model. Afterwards, using VOD, VCF and SSM in each year, we performed 1/12° resolution AGB simulations over 2003–2020 along with ten-fold cross-validations, and adopted the mean of ten independent simulations. We also calculated the 'calibration factor' which is defined as the ratio of resampled AGBbenchmark-2000 (i.e., the training target) to the simulated AGB in 2003 in every grid. Then, we multiplied the annual 1/12° resolution AGB in China during 2003–2020 with the grid-specific 'calibration factor'.

For the next step, we downscaled the 1/12° resolution AGB to 1/120°. Here, it is assumed that within a grid cell, the heights of trees are similar, while the short vegetation's heights are also similar. So, within a 1/12° grid cell, the AGB per tree cover (TC) and AGB per short vegetation cover (SC) can both be considered constants. Hence, we performed a binary linear regression between the AGBbenchmark-2000s value in each 1/120° pixel within the grid cell and the corresponding VCF (TC and SC) values. The intercept (i.e., constant term) was excluded, so the derived two regression coefficients can represent

https://doi.org/10.5194/essd-2022-286
Preprint. Discussion started: 26 September 2022

the mean values of AGB per TC and per SC in the grid cell. For more than 75% of all grid cells, the regression R^2 exceed 0.5. Since VCF indicates the coverage of pure tree and non-tree vegetation, AGB per TC should be higher than that per SC. Therefore, for grid cells where the derived AGB per TC was smaller than the AGB per SC, grids where either one of the regression coefficients was negative, or those without very significant regressions (i.e., $p>0.01$ or $R^2<0.1$), the regression was considered invalid. The AGB per TC and AGB per SC in those grid cells were filled later by searching for nearby valid regression results, while the R^2 values of those valid regressions were applied as the weights in averaging the nearby valid values. The maps of AGB per TC and per SC in 2003 are shown in Figure S3. By integrating these data with pixel-scale VCF, we calculated the AGB of all woody vegetation in each 1/120° pixel, which was averaged to the AGB at 1/12° resolution. Accordingly, the ratio of the grid-scale AGB calculated in the first step to the aggregated AGB derived in this step can be used to further calibrate the high-resolution AGB data. Finally, by repeating the procedures, we mapped woody AGB in China at 1/120° resolution from 2003 to 2020.

2.4 Mixed-pixel AGB decomposition- towards scale matching

We mapped AGB in China at 1/120° pixel resolution, which is quite larger than the scale of plot measurements. The collected plot-level data usually represent the AGB and BGB per area in a forest or shrubland with basically uniform landscapes (i.e., the density of trees/shrubs is even in the plot, which can be either low or high). However, within a pixel, forests, shrubs, crops, herbs and bare ground may coexist. It is known that the relationship between BGB and AGB in forests differs from that in shrublands. Generally, shrub species have a much higher RSR than trees (Qi et al., 2019; Tang et al., 2018). Hence, we tried to solve that ‘mixed-pixel problem’ by decomposing the simulated AGB in woody regions into the AGB per forestland area and the AGB per shrubland area. Then, we applied the respective relationships between BGB and AGB to transform the decomposed per-area AGBs into per-area BGBs for different types of forests and shrublands. Afterwards, we multiplied the per-area BGBs with the corresponding area and summed the products (i.e., all forestlands’ BGB and shrublands’ BGB). By this method, we basically achieved scale matching between remote sensing and plot-level observations.

https://doi.org/10.5194/essd-2022-286
Preprint. Discussion started: 26 September 2022

AGB decomposition generally followed the idea we proposed in a previous article (Chen et al., 2019b). Specifically, in woody grids, we counted the numbers of pixels with forests (i.e., pixels in which the forestland area percentage was >10% according to the CGLS-LC) and those with shrublands (shrubland area percentage >10%). For grid cells where there were at least 50 pixels with forestland and 50 pixels with shrubland, we performed a binary linear regression without intercept between all these pixel-scale AGB data and the area percentages of forestland and shrubland in every woody pixel. Afterwards, the average per-area BGB for forestland and shrubland in woody grid cells can be estimated as the corresponding regression coefficients. However, the regression was supposed invalid when either regression coefficient was negative, or the significance p-value exceeded 0.05, or R^2 was below 0 (R^2 can be negative for regressions without constants due to the potential significant bias in AGB data). For these grids, a constant term was further added to the regression if a valid result could be derived under this situation. Specifically, for 1/12° grids with less than 50 pixels with forests, but the pixels with shrubland are sufficient, we can reliably estimate the AGB per area shrubland as the ratio of grid average AGB to the mean shrubland area percentage in the grid. Similarly, the forestland per area AGB in grids with only enough pixels with forests can be estimated by simply neglecting the few shrubs. According to Figure S4a~b, complete AGB decomposition was achieved in 36% of all grids with enough woody pixels, and the grid cells with reliable AGB estimates accounted for 61%. The invalid decompositions composed only 3%, which were filled later by sequentially searching and averaging nearby valid results (88% of the valid regressions are with R^2 higher than 0.5, see Figure S4c~d). Subsequently, we deleted both the highest and lowest 2.5% values of all gridded per-area AGB estimates in China, and then filled those values. Finally, a mean filter with a window size of 3×3 was applied for spatial smoothing. The final maps of AGB per area forestland and that per shrubland area in around 2017 (note: CGLS-LC data represent the land cover around 2017) are shown in Figure S5. Within a grid cell, the per-area forestland's AGB is usually (71% in China) higher than the corresponding per-area shrubland AGB, except in mountains around the Sichuan Basin and some karst regions in southwestern China where shrubs are probably much denser than trees. Because the average forestland area percentage in woody grids in China (55%) is greater than the CGLS-LC's mean shrubland area percentage (13%), the average forestlands' AGB calculated based on the decomposition result (63.4 t ha^{-1}) is much larger than the mean shrublands' AGB (11.6 t ha^{-1} in around 2017), which is reasonable.

https://doi.org/10.5194/essd-2022-286
Preprint. Discussion started: 26 September 2022

After the decomposition, some per-area AGBs were filled-in values, while some were derived from linear regressions with intercepts. Therefore, the sum of forestland AGB and shrubland AGB in approximately 2017 may not be equal to the total grid AGB at the same time before decomposition. In addition, the sum of the decomposed AGBs in 2017 was obviously different from the pre-decomposed AGB in other years. To solve this problem, we defined and calculated another 'calibration factor' as the ratio of the simulated grid-scale AGB in any year from 2003 to 2020 before mixed-pixel decomposition to the grid's AGB in 2017 after the decomposition. Accordingly, by referring to the per-area forestland/shrubland AGB in 2017 and this 'calibration factor' in each separate year, we could decompose the annual simulated pixel-scale AGB into the 1/120° resolution AGBs of forests and shrublands and the per-area forestland/shrubland's AGB over the whole study period.

2.5 BGB mapping in China during 2003–2020 based on its relationship with AGB

In this study, we collected 8729 and 302 records of both AGB and BGB in forest and shrubland plots, respectively, throughout China (section 2.1). For forest plots, the BGB~AGB relationship follows: log (BGB)=0.93×log (AGB)−0.51, while the relationship for shrubland plots follows: log (BGB)=0.96×log (AGB)−0.20, and the regression R^2 are 0.92 and 0.85, respectively (Figure S6). The number of forest plots is large enough, and the forest type (main species) and stand age information are both available at 8182 plots (~94% of all forest plots), including both natural forest plots and plantation forest plots (pines, Eucalyptus, rubbers, bamboos, etc.). Therefore, we trained an RF model for estimating per-area forestland's BGB annually.

In the RF model, the training target is the per-area BGB at 8182 forest plots, while the predictors included not only forest plots' per-area AGB, forest type (hereinafter FOR_T), stand age, but also mean annual temperature (MAT), temperature seasonality (standard deviation of monthly temperature×100, abbreviated as Tsea), mean annual precipitation (MAP) and precipitation seasonality (coefficient of variation of monthly precipitation, Psea). These climatic factors can be obtained from the corresponding papers, or estimated from the WorldClim v2.1 dataset (Fick and Hijmans, 2017). In this study, FOR_T includes evergreen broadleaf forest (EBF), deciduous broadleaf forest (DBF), evergreen needleleaf forest (ENF), deciduous needleleaf forest (DNF), and mixed forest (MF), and was determined based on the major tree species in the plot. After the RF

https://doi.org/10.5194/essd-2022-286
Preprint. Discussion started: 26 September 2022

training, to simulate grid-scale per-area forestland's BGB annually, apart from importing WorldClim v2.1's MAT, Tsea, MAP, Psea and the decomposed per-area forestland AGB in each year into the RF model, we also inputted the forest stand age map for China (Zhang et al., 2017) and the annual forest type map during 2003–2020, which was determined from the ESA CCI's global 300 m resolution annual land cover classification v2.0.7cds~v2.1.1 (Li et al., 2018).

Because shrubland plots are relatively limited, and the species and stand age information was hardly provided, we directly converted the decomposed shrublands' per-area AGB into the per-area BGB during 2003–2020 using the above regression relationship. Finally, by referring to the forestland and shrubland area percentages in the CGLS-LC dataset, we mapped the annual woody BGB in China at 1/120° resolution.

In addition, we also calculated the relative errors and uncertainties of AGB and BGB in each year during 2003–2020 (see section 3.4).

2.6 Data comparison and verifications

Apart from cross-validations based on woody plots' AGB and BGB measurements over China, we further verified our AGB and BGB estimates by referring to the results of Tang et al., who conducted a methodologically consistent field campaign involving 7800 forest plots and 1200 shrubland plots throughout China and then utilized the random forest approach to spatially map AGB and BGB (Tang et al., 2018). Although the plot measurements are not publicly available, various statistics of this national official product were reported, e.g., the AGB, BGB and RSR for each woody vegetation type. Therefore, using the discrete land cover classification map in the CGLS-LC dataset, we classified China's woody ecosystems into six woody ecosystem types, i.e., EBF, DBF, ENF, DNF, MF and shrubland (SHR) ecosystems, according to the majority in every pixel (Figure S7). The EBF, DBF, ENF, DNF, MF and SHR ecosystems account for 59.6%, 18.4%, 15.3%, 6.1%, 0.1% and 0.5%, respectively, of the total woody area in China. Because the MF and SHR ecosystems both have very limited areas, this study just compares the AGB and BGB per area among the four major forest ecosystems in China. Similarly, the change in woody biomass or carbon stock in China can be verified by several measurements and remote sensing-based studies (Fang et al., 2018; Qiu et al., 2020; Xu et al., 2018).

https://doi.org/10.5194/essd-2022-286
Preprint. Discussion started: 26 September 2022

We also compared the calculated spatial pattern of woody biomass and its trend against that of existing global/regional long-term woody biomass datasets, including the well-received global long-term AGB between 1993~2012 (Liu et al., 2015) and an updated woody biomass dataset covering 2001~2019 (Xu et al., 2021).

Finally, to justify the random forest models for biomass and allocation predictions, we drew partial dependence plots (PDPs) in MATLAB R2021a® to show the marginal effect that one predictor has on the training target (e.g., BGB at forest plots) from a machine learning model (Hastie et al., 2009). Here, for each predictor, we excluded the extreme values (the lowest 1% and the highest 1%) before calculating the corresponding PDP to ensure its robustness. Ten RF trainings were performed to derive the mean PDP values as well as the standard deviations.

3 Results and discussion

3.1 Model development and Evaluation

In the first step, i.e., the benchmark woodland AGB mapping, when ATLAS data-derived canopy height was applied as an additional predictor in the RF model apart from the three biomass datasets (see section 2.1), the number of data points available for training was 1392, and the predicted R-square (R^2) according to the ten-fold cross validation was 0.49±0.06 (mean ± standard deviation). The training efficiency is limited by the potential errors in plot-level AGB records as well as the CGLS-LC's land cover fraction maps, and the scale difference between satellite and plot-level observations. Although introducing climatic and topographic variables as predictors could increase the R^2 of ten-fold cross validation, these variables contain high spatial autocorrelation, and thus even an elevated R^2 cannot indicate a higher predictive performance (Ploton et al., 2020). According to a test addressing the relative contribution of the four predictors, GLASS-Biomass dataset contributed most to the woody AGB mapping (35%), followed by GlobBiomass (24%), CCI-Biomass (22%) and ATLAS-derived tree volume (19%). When GEDI-derived and GLAS-derived wood volumes were respectively used, the available data points increased to 3842 and 2286, but the mean R^2 values were 0.36, because the direct observations of ICESAT-2 were supposed to be more accurate than the canopy heights estimated through machine learning by GLAD or Simard et al. After

https://doi.org/10.5194/essd-2022-286
Preprint. Discussion started: 26 September 2022

combining these three sets of AGB simulations, the R^2 between the resulting benchmark AGB map for China (Figure S1c) and the upscaled plots' AGB was 0.56, while the RMSE was 40.38 t ha^{-1} (Figure S1b). When comparing the GlobBiomass, CCIBiomass and GLASS-Biomass datasets against the upscaled plots' AGB, the R^2 were 0.19, 0.13 and 0.18, respectively, while the RMSE were 69.2, 69.3 and 84.1 t ha^{-1}. Therefore, the benchmark map of AGB in China has been significantly improved.

In the second step, i.e., long-term continuous AGB mapping (section 2.3), with a ten-fold cross-validation, the RF model's predictive R^2 and RMSE were 0.79±0.01 and 16.7±0.33 t ha^{-1}, respectively. Vegetation continuous fields (VCF) contributed most to the training efficiency (tree cover and all vegetation cover contributed 39% and 17%, respectively). Mean and median vegetation optical depth (VOD) values both contributed 17% to the training efficiency, whereas mean surface soil moisture accounted for 10% (methods are in section 2.3).

The RF model designed for woody plots' BGB estimation (see section 2.5) achieved a predictive R^2 of 0.89±0.02, and the RMSE was 6.3±0.5 t ha^{-1}. AGB explained 53% of the BGB's variation among different woody plots. Long-term climate backgrounds, i.e., mean annual temperature, temperature seasonality, annual precipitation and precipitation seasonality accounted for 8%, 6%, 8% and 7%, respectively. Forest type and stand age also contributed 12% and 8% to the training efficiency, indicating that the effects of these factors are nonnegligible. The selection of predictors of BGB basically followed the existing knowledge (Huang et al., 2021), and the seasonality of temperature and precipitation made sense in the prediction (see Text S1). On the other hand, although previous studies incorporated many edaphic factors as predictors of BGB (Huang et al., 2021), by comparing the training efficiencies when whether these edaphic factors are incorporated, we could justify the reasonability of our simplified set of predictors (Text S1).

We also explored how different factors influence AGB and BGB among woody plots in China. Of the biotic and abiotic factors included in our model, partial dependence plots (PDPs, Figure 2a~c) show that stand age is the main driver of AGB. However, with forest aging, forest growth gradually stops, conforming with common knowledge (Xu et al., 2010). Woody AGB also increases significantly with precipitation, but water availability does not constrain biomass in humid regions with annual precipitation above 1500 mm, and temperature did not significantly affect AGB at large scales. These findings are in

https://doi.org/10.5194/essd-2022-286
Preprint. Discussion started: 26 September 2022

line with previous studies (Stegen et al., 2011).

According to the collected woody plots' data, AGB is a key driver of BGB (Figure 2d~g). Yet, RSR changes among different forest growth stages, decreasing in general as reported (Mokany et al., 2006). The overall negative impact of mean temperature on BGB or RSR agrees with the mechanism that higher heat promotes nutrient accessibility (Luo et al., 2012; Ma et al., 2021), and increases the turnover rates of roots at a higher magnitude than stems (Reich et al., 2014). The 'U-shaped' relationship between precipitation and belowground biomass allocation follows the 'optimal biomass allocation' theory, because arid climates promote root extension yet too heavy rainfall reduces nutrient availability through leaching and dilution effect (Luo et al., 2012). Other factors, including temperature seasonality, precipitation seasonality and forest type, have supplementary effects on the biomass allocation (Figure S8).

https://doi.org/10.5194/essd-2022-286
Preprint. Discussion started: 26 September 2022

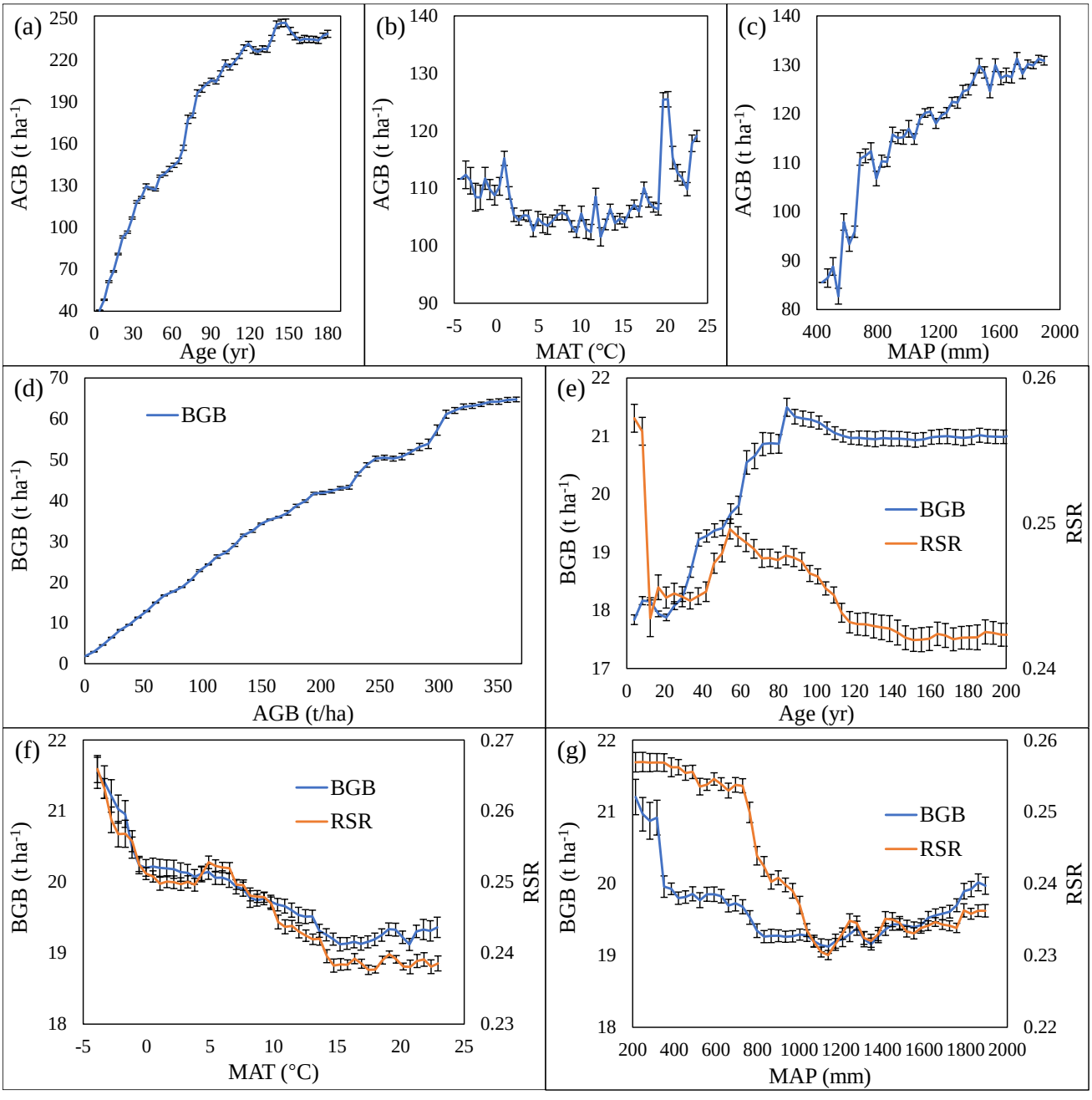

400 **Figure 2: Influence of key factors on woody plots' above- and belowground woody biomass in China. (a~c) Partial effects of (a) forest age; (b) mean annual temperature (MAT) and (c) mean annual precipitation (MAP) on AGB in all qualified woody plots; (d~g) partial influences of (d) AGB; (e) stand age; (f) MAT and (g) MAP on BGB and RSR values of all qualified woody plots. The error bars represent the standard deviations of the ten-fold trainings. We did not draw the PDP for the impact of AGB on RSR, since the dividend of RSR calculation is AGB.**

https://doi.org/10.5194/essd-2022-286
Preprint. Discussion started: 26 September 2022

3.2 Total woody biomass, allocation and change in China

Between 2003 to 2020, the total woody biomass in forestlands and shrublands in China were 28.4 (mean) ±1.8 (standard deviation) Pg and 2.3±0.2 Pg dry matter (DM), respectively (Table 1), while the total woody AGB and BGB were 24.4±1.6 Pg and 6.2±0.4 Pg. The mean RSR for forests (0.24) and that of all woody areas in China (0.26) are both slightly lower than the global average values of approximately 0.25 and 0.3, respectively (Ma et al., 2021; Huang et al., 2021). Separated by forest types, evergreen conifer forest (ENF) occupies the highest woody total biomass per unit area (175.1 t ha^{-1}), followed by 136.4 t ha^{-1} in the evergreen broadleaf forest (EBF), whereas deciduous forests (DBF and DNF) harbor 119.7 and 122.3 t ha^{-1}, respectively (Figure 3a). By contrast, deciduous forests in northern China (see Figure S7 for the distribution of forest ecosystems) occupy higher mean RSR values (Figure 3a).

Woody biomass across China increased by an average rate of 363.9±11.2 Tg yr^{-1} (DM) during 2003–2020, equaling a vegetation carbon sink of approximately 163.8±5.9 TgC yr^{-1} (assuming a carbon density to biomass ratio of 0.45 (Xu et al., 2018)). Changes in forestland AGB, forestland BGB, shrubland AGB and shrubland BGB account for 73.8%, 7.1%, 15.5% and 3.6%, respectively, of the total woody biomass trend. Apart from visible declines from 2010 to 2011 and from 2016 to 2017, China has undergone a continuous increase in woody biomass ($p<0.01$) during 2003–2020, and the biomass gains were the greatest from 2014 to 2016 (Figure 3b).

Our estimates of woody biomass and its trend are generally consistent with previous results in China obtained using both satellite observation and massive field measurements (Table 1). Yet, differences occur in some aspects. For example, as the grass-dominated pixels are excluded in this study, the mean RSR for Chinese shrubs (including those in grass-dominated pixels) was reported as 0.71 (Tang et al. 2018), slightly higher than our estimate of 0.53 for shrubland ecosystems in China. Moreover, regarding trees' occurrence in shrublands, the shrublands' woody biomass and RSR values in this study refer to a mosaic of shrubs and some trees.

Table 1. Basic statistics of the calculated woody biomass in China and the agreement with those reported previously (the ratio of carbon density to biomass is set to 0.45 (Xu et al., 2018)).

https://doi.org/10.5194/essd-2022-286
Preprint. Discussion started: 26 September 2022

Variables related to woody biomass	Our estimate (mean value in 2003–2020)	Previous high-quality estimates	Reference
Forestland AGB in China	22.9 Pg	18.7 Pg	(Tang et al., 2018)
Forestland BGB in China	5.5 Pg	4.6 Pg	
Shrubland AGB in China	1.5 Pg	0.9 Pg	
Shrubland BGB in China	0.8 Pg	0.7 Pg	
Woody biomass in China	30.7 Pg	24.9~26.4 Pg	(Tang et al., 2018; Xu et al., 2018)
Forestland RSR in China	0.24	0.23~0.25	(Jiang and Wang, 2017; Tang et al., 2018)
Shrubland RSR in China	0.53	0.71	(Tang et al., 2018)
ENF's per-area AGB	143.5 t ha^{-1}	~122 t ha^{-1}	(Tang et al., 2018)
EBF's per-area AGB	109.5 t ha^{-1}	~109 t ha^{-1}	
DBF's per-area AGB	92.2 t ha^{-1}	~87 t ha^{-1}	
DNF's per-area AGB	91.5 t ha^{-1}	~98 t ha^{-1}	
All forests' per-area AGB	109.3 t ha^{-1}	99~112 t ha^{-1}	(Tang et al., 2018; Yin et al., 2015)
Forests' per-area total biomass	137.3 t ha^{-1}	124~144 t ha^{-1}	(Tang et al., 2018; Yao et al., 2018)
ENF's RSR	0.22±0.03	0.24	(Tang et al., 2018)
EBF's RSR	0.25±0.04	0.22	
DBF's RSR	0.30±0.03	0.28	
DNF's RSR	0.34±0.04	0.31	
Annual woody carbon stock increase	163.8±5.9 TgC yr^{-1}	120.2 TgC yr^{-1} (2000~2010)	(Fang et al., 2018)
		178 TgC yr^{-1} (2020~2030)	(Tang et al., 2018)
		170 TgC yr^{-1} (2000s~2040s)	(Yao et al., 2018)
Annual forests' carbon stock increase	146.2~163.8 TgC yr^{-1}	153.6 TgC yr^{-1} (2003–2020)	(Qiu et al., 2020)

https://doi.org/10.5194/essd-2022-286
Preprint. Discussion started: 26 September 2022

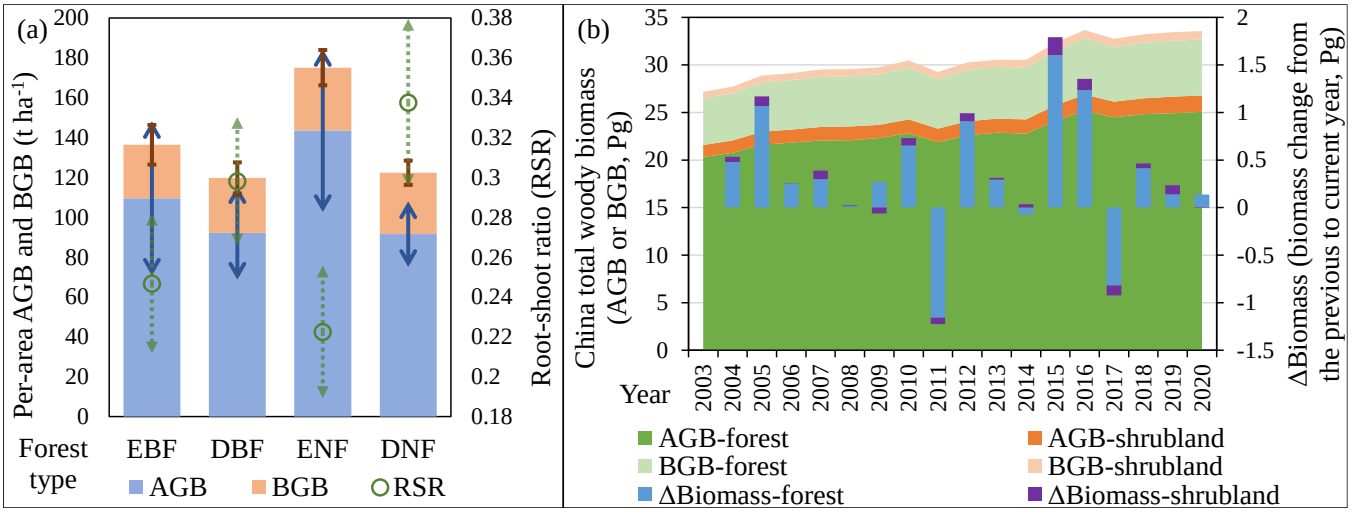

Figure 3. Woody biomass allocation and biomass change in China during 2003–2020: (a) per-area AGB and BGB, as well as RSRs of different forest ecosystems in China. The blue, red and green error bars are the standard deviations of AGB, BGB and RSR in China; (b) the interannual changes of total forestland' AGB (AGB-forest), shrubland' AGB (AGB-shrubland), forestland' BGB (BGB-forest), shrubland' BGB (BGB-shrubland). Biomass changes (ΔBiomass) in forests and shrublands from the previous to the current year are represented by blue and purple columns.

3.3 Updated spatial hotspots of woody biomass amount and trend in China

The highest per-area woodland biomass is observed in the southwest of China, especially south Tibet. Woody biomass is also high in parts of the Qinling Mountains, Hengduan Mountains, Hainan and Taiwan islands (Figure 4a). Hence, woody biomass was highest in the south < 34°N, followed by the northeast forests, and lowest in the mid-latitudes, 38–40°N (Figure 4b). Above- and belowground woody biomass allocation varies significantly among regions. RSR is highest in northeastern conifer forests and northern China's deciduous forest. The southwest karsts also have higher RSR than its surroundings due to high shrubland biomass (Figure 4c and Figure S5b). Woody pixels' RSR ranges from 0.17 to 0.42 across China, with 67% of pixels having a RSR of 0.2–0.3 (Figure 4d). The strongest biomass increases were found in central to southern China, including the southern part of the Loess Plateau, the Qinling Mountains, the southwest karst region and southeastern forests. Declines in woody biomass only occurred in some mature natural forests, e.g., those in the Greater Khingan Mountain, Hengduan Mountains and South Tibet (Figure 4e). 59.8% of woody areas in China showed significant biomass gains (Figure 4f).

https://doi.org/10.5194/essd-2022-286
Preprint. Discussion started: 26 September 2022

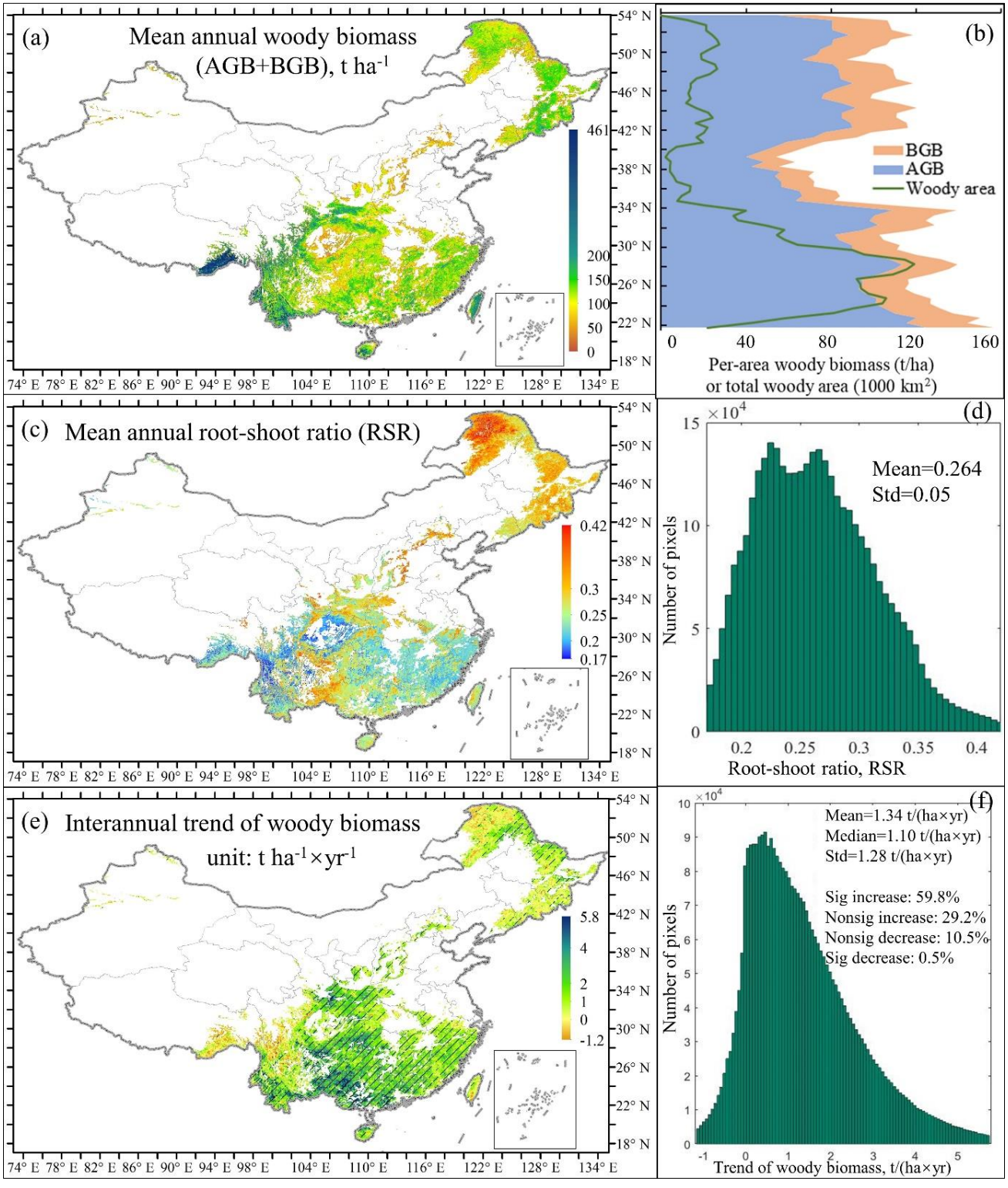

https://doi.org/10.5194/essd-2022-286
Preprint. Discussion started: 26 September 2022

Figure 4. Maps of woody biomass amount, allocation and trend in China during 2003–2020. (a) Spatial pattern of woody total biomass in China; (b) the latitudinal pattern of per-area woody AGB, BGB and total woody area in China (woody areas below 22°N are limited); (c~d) map of woody vegetation's RSR and its histogram; (e~f) map of the woody biomass trend and its histogram. Shaded areas in trend maps indicate statistically significant at the 95% confidence level, while the basic statistics of all woody pixels' biomass amount and trend are labelled in the subfigures (Sig/Nonsig: significant/nonsignificant trends at the 95% confidence level).

In agreement with our results (AGB: 24.4±1.6 Pg, total biomass: 30.7±2.0 Pg), previous studies estimated a total woody AGB in China of 23.4±0.6 Pg after 2003 (Liu et al., 2015) and a total woody biomass of 29.4±1.1 Pg during 2003~2019 (Xu et al., 2021). However, the spatial pattern inferred here markedly differ compared with these previous estimates. We predict higher woody biomass in the central-south and southwest China but lower biomass values in the northern and northwest regions (Figure S9a~f). The spatial pattern of our AGB map agrees well with that of recent high-quality China's forest AGB maps which were developed by integrating Lidar, P-band SAR and forest inventory data (Su et al., 2016; Huang et al., 2019), with the correlation coefficients both reaching 0.73. For Liu et al. (2015)'s and Xu et al. (2021)'s dataset, the spatial pattern correlations with those improved AGB maps are 0.35~0.50 and 0.27~0.37, respectively (Figure S10). The mean woody AGB in eight provinces of southern China was 92~104 t ha^{-1} (Tong et al., 2020), close to our estimate of 85~110 t ha^{-1}. Forest inventory indicated a tree biomass of 1.92 Pg in Tibet (Sun et al., 2016) where our result was 1.86 Pg yet the two existing long-term datasets predicted 1.26~1.52 Pg. Moreover, the reduced spatial variation in biomass estimated in this study compared to Liu et al. (Figure S9a) indicate much lower random noises.

The interannual variation in woody AGB in China according to Liu et al. (2015) and that of total woody biomass according to Xu et al. (2021) are both highly correlated with our results (r= 0.76 and 0.95). Liu et al. predicted a woody AGB increasing rate of 186±79.6 Tg yr^{-1} ($p<0.01$), similar to our estimate of 236±117 Tg yr^{-1} over 2003~2012; while Xu et al. indicated a biomass trend of 219.4±79.6 Tg yr^{-1} ($p<0.01$) from 2003 to 2019, lower than the rate of 368±69.9 Tg yr^{-1} in this study (Figure S11a, c). Spatially, this study predicted an obviously faster biomass gains in southern China than their datasets (Figure S11). Reforestation and forest management led to a short term extensive carbon sequestration in southern China, which was estimated as 220±100 Tg AGB yr^{-1} during 2002~2017 by developing a regional RF model between MODIS

https://doi.org/10.5194/essd-2022-286
Preprint. Discussion started: 26 September 2022

reflectance data and a global benchmark AGB map (Tong et al., 2020), close to our estimate of 200±58 Tg AGB yr^{-1}. The high ecosystem carbon sink in central to south China and southwestern China has been shown by atmospheric inversions as well (Wang et al., 2020; Yang et al., 2021).

Accordingly, by fusing low-frequency active, passive microwaves and the advanced LiDAR-derived canopy heights under the reference of extensive field measurements, this study could generate updated estimates on the spatial hotspots of woody biomass and its trends in China.

3.4 Uncertainties of the woody biomass dataset and future prospects

The uncertainties of AGB in this study came from four sources: 1) the improved benchmark AGB map for China; 2) the extension of AGB time series based on the long-term integrated VOD and high/short vegetation coverage datasets; 3) downscaling of coarse resolution AGB; and 4) the AGB decomposition process. The uncertainty in BGB was composed of the error within the AGB time series and the prediction uncertainty of the models that transform AGB to BGB. The details for the calculation of each source of error are in Text S2. Finally, the annual AGB and BGB's relative error can be calculated as the square root of the sum of squares of all relative errors, which is referred to as the 'error propagation rule' when assuming that each error is independent and random (Huang et al., 2021). By multiplying the annual AGB or BGB map with the corresponding relative error, we mapped the AGB and BGB's uncertainties in China annually during 2003–2020. As shown in Figure S12, the spatial patterns of the relative errors of AGB and BGB are similar. Relative errors were lower in the pure forests located in northeast China and the south Tibet, and high in the mixed forest and shrublands in the southwest karst regions and part of North China.

A recent study revealed that the variation in VODs is correlated with not only biomass, but also soil moisture availability (Konings et al., 2021). To alleviate this source of uncertainty as much as possible, we have incorporated the satellite-based surface soil moisture dataset to account for the impact from the interannual variation in water content per biomass. In addition, we have included optical-based vegetation continuous fields in predicting the interannual variation in woody biomass, which turned out to be the variable with the highest contribution (56%). In fact, the interannual variation in Chinese

https://doi.org/10.5194/essd-2022-286
Preprint. Discussion started: 26 September 2022

woody biomass according to this study is highly correlated (r=0.95) with that calculated independent of microwave-based VOD (Xu et al., 2021).

Next, the variation in climatic conditions in a short term may have some influences on that in BGB, but explicit knowledge on this effect is lacking. Instead, woody vegetation BGB is much more driven by AGB (vegetation density), as indicated by the very strong relationship between BGB and AGB ($R^2 \geq 0.85$). Moreover, the long-term climatic background is expected to have a stronger influence on the RSR of perennial woody plants than the meteorological conditions in only a few years, since above- and belowground biomass allocation is the result of plants' long-term adjustment to the environment (Qi et al., 2019). Accordingly, it is reasonable not to consider the impact of the specific climatic conditions in a year on the variation in BGB.

The collected plot AGB measurements span many years, mostly between 1990 and 2010. So, it is assumed that the machine learning-derived benchmark AGB map roughly stand for the AGB status around 2000 (see section 2.1), and thus we linked it to the VOD in 2003, the first year of our study period, rather than that in any other year (section 2.3). This assumption may contribute to some uncertainties in the absolute values of annual AGB in some parts of China, but will not have much impact on the spatial pattern and temporal variation of woody biomass.

In near future, P-band microwave sensors, which have higher penetrability into the canopy than L-band microwaves, will further improve the AGB mapping. For example, BIOMASS, a fully polarimetric P-band SAR, is scheduled to be launched in 2022 (Le Toan et al., 2011). Therefore, in the future the relationship between P-band microwave retrievals and biomass should be addressed, as well as the calibration of historical AGB datasets (e.g., the long-term AGB dataset in this study) against the P-band SAR-based AGB benchmark map to extend the time series. On the other hand, more in-situ AGB and BGB measurements in larger plots and in approximate years are needed to further improve the estimation of belowground biomass allocation.

Data availability

Annual maps of woodland AGB and BGB in China is available at https://doi.pangaea.de/10.1594/PANGAEA.936276 (Chen,

https://doi.org/10.5194/essd-2022-286
Preprint. Discussion started: 26 September 2022

2021). Other datasets that made this research possible and the related references are attached in Supplementary Information-Text S3.

Funding and acknowledgements

This work was supported by the National Key Research and Development Program of China (2017YFA0604700), National Science Foundation of China (41991233) and the Chinese Academy of Sciences (QYZDY-SSW-DQC025). We are grateful to all the data contributors, especially Yuan Zhang and Huabing Huang for sharing the forest stand age map and forest aboveground biomass map in China to us.

Author contributions

Y.C designed and conducted the research. B.F and X.F funded the research. Y.Z wrote the draft of the manuscript; X.F and all other authors read and revised the manuscript.

Competing interests

The authors declare that they have no conflict of interest.

Acknowledgements

We are grateful to all the data contributors, especially Yuan Zhang and Huabing Huang for sharing the forest stand age map and forest aboveground biomass map in China to us.

Financial support

This work was supported by the National Key Research and Development Program of China (2017YFA0604700), National Science Foundation of China (41991233) and the Chinese Academy of Sciences (QYZDY-SSW-DQC025).

https://doi.org/10.5194/essd-2022-286
Preprint. Discussion started: 26 September 2022

References

Baret, F., Weiss, M., Lacaze, R., Camacho, F., Makhmara, H., Pacholcyzk, P., and Smets, B.: GEOV1: LAI and FAPAR essential climate variables and FCOVER global time series capitalizing over existing products. Part1: Principles of development and production, Remote. Sens. Environ., 137, 299-309, https://doi.org/10.1016/j.rse.2012.12.027, 2013.

Bouvet, A., Mermoz, S., Le Toan, T., Villard, L., Mathieu, R., Naidoo, L., and Asner, G. P.: An above-ground biomass map of African savannahs and woodlands at 25m resolution derived from ALOS PALSAR, Remote Sens. Environ., 206, 156-173, https://doi.org/10.1016/j.rse.2017.12.030, 2018.

Buchhorn, M., Lesiv, M., Tsendbazar, N.-E., Herold, M., Bertels, L., and Smets, B.: Copernicus Global Land Cover Layers—Collection 2, Remote Sens., 12, https://doi.org/10.1029/2018EF00089010.3390/rs12061044, 2020.

Cammalleri, C., Verger, A., Lacaze, R., and Vogt, J. V.: Harmonization of GEOV2 fAPAR time series through MODIS data for global drought monitoring, Int. J. Appl. Earth Obs., 80, 1-12, https://doi.org/10.1016/j.jag.2019.03.017, 2019.

Cartus, O., Santoro, M., and Kellndorfer, J.: Mapping forest aboveground biomass in the Northeastern United States with ALOS PALSAR dual-polarization L-band, Remote Sens. Environ., 124, 466-478, https://doi.org/10.1016/j.rse.2012.05.029, 2012.

Chen, C., Park, T., Wang, X., Piao, S., Xu, B., Chaturvedi, R. K., Fuchs, R., Brovkin, V., Ciais, P., Fensholt, R., Tømmervik, H., Bala, G., Zhu, Z., Nemani, R. R., and Myneni, R. B.: China and India lead in greening of the world through land-use management, Nat. Sustain., 2, 122-129, https://doi.org/10.1029/2018EF00089010.1038/s41893-019-0220-7, 2019a.

Chen, Y.: Longterm above- and belowground woody biomass maps in China from 2003 to 2020 [dataset], https://doi.pangaea.de/10.1594/PANGAEA.936276, 2021.

Chen, Y., Feng, X., and Fu, B.: An improved global remote-sensing-based surface soil moisture (RSSSM) dataset covering 2003–2018, Earth Syst. Sci. Data, 13, 1-31, https://doi.org/10.1029/2018EF00089010.5194/essd-13-1-2021, 2021.

Chen, Y., Feng, X., Fu, B., Shi, W., Yin, L., and Lv, Y.: Recent Global Cropland Water Consumption Constrained by Observations, Water Resour. Res., 55, 3708-3738, http://doi.org/10.1029/2018WR023573, 2019b.

Dubayah, R., Blair, J. B., Goetz, S., Fatoyinbo, L., Hansen, M., Healey, S., Hofton, M., Hurtt, G., Kellner, J., Luthcke, S., Armston, J., Tang, H., Duncanson, L., Hancock, S., Jantz, P., Marselis, S., Patterson, P. L., Qi, W., and Silva, C.: The Global Ecosystem Dynamics Investigation: High-resolution laser ranging of the Earth's forests and topography, Sci. Remote Sens., 1, 100002, https://doi.org/10.1016/j.srs.2020.100002, 2020.

Enquist Brian, J. and Niklas Karl, J.: Global Allocation Rules for Patterns of Biomass Partitioning in Seed Plants, Science, 295, 1517-1520, https://doi.org/10.1029/2018EF00089010.1126/science.1066360, 2002.

Fang, J., Yu, G., Liu, L., Hu, S., and Chapin, F. S.: Climate change, human impacts, and carbon sequestration in China, P. Natl. Acad. Sci. USA, 115, 4015, https://doi.org/10.1029/2018EF00089010.1073/pnas.1700304115, 2018.

Fick, S. E. and Hijmans, R. J.: WorldClim 2: new 1-km spatial resolution climate surfaces for global land areas, Int. J. Climatol., 37, 4302-4315, https://doi.org/10.1029/2018EF00089010.1002/joc.5086, 2017.

Frappart, F., Wigneron, J.-P., Li, X., Liu, X., Al-Yaari, A., Fan, L., Wang, M., Moisy, C., Le Masson, E., Aoulad Lafkih, Z., Vallé, C., Ygorra, B., and Baghdadi, N.: Global Monitoring of the Vegetation Dynamics from the Vegetation Optical Depth

(VOD): A Review, Remote Sens., 12, https://doi.org/10.1029/2018EF00089010.3390/rs12182915, 2020.

Guo, J., Guo, Y., Chai, Y., Liu, X., and Yue, M.: Shrubland biomass and root-shoot allocation along a climate gradient in China, Plant Ecol. Evol., 154, 5-14, https://doi.org/10.1029/2018EF00089010.5091/plecevo.2021.1570, 2021.

Guo, Q. and Ren, H.: Productivity as related to diversity and age in planted versus natural forests, Global Ecol. Biogeogr., 23, 1461-1471, https://doi.org/10.1111/geb.12238, 2014.

Hastie, T., Tibshirani, R., and Friedman, J.: The Elements of Statistical Learning Data Mining, Inference, and Prediction, Second Edition, Section 10.13.2, Springer2009.

Hu, T., Su, Y., Xue, B., Liu, J., Zhao, X., Fang, J., and Guo, Q.: Mapping Global Forest Aboveground Biomass with Spaceborne LiDAR, Optical Imagery, and Forest Inventory Data, Remote Sens., 8, https://doi.org/10.1029/2018EF00089010.3390/rs8070565, 2016.

Huang, H., Liu, C., Wang, X., Zhou, X., and Gong, P.: Integration of multi-resource remotely sensed data and allometric models for forest aboveground biomass estimation in China, Remote. Sens. Environ., 221, 225-234, https://doi.org/10.1016/j.rse.2018.11.017, 2019.

Huang, Y., Ciais, P., Santoro, M., Makowski, D., Chave, J., Schepaschenko, D., Abramoff, R. Z., Goll, D. S., Yang, H., Chen, Y., Wei, W., and Piao, S.: A global map of root biomass across the world's forests, Earth Syst. Sci. Data, 13, 4263-4274, https://doi.org/10.1029/2018EF00089010.5194/essd-13-4263-2021, 2021.

Jackson, T. J. and Schmugge, T. J.: Vegetation effects on the microwave emission of soils, Remote. Sens. Environ., 36, 203-212, https://doi.org/10.1016/0034-4257(91)90057-D, 1991.

Jiang, Y. and Wang, L.: Pattern and control of biomass allocation across global forest ecosystems, Ecol. Evol., 7, 5493-5501, https://doi.org/10.1002/ece3.3089, 2017.

Konings, A. G., Piles, M., Das, N., and Entekhabi, D.: L-band vegetation optical depth and effective scattering albedo estimation from SMAP, Remote. Sens. Environ., 198, 460-470, https://doi.org/10.1016/j.rse.2017.06.037, 2017.

Konings, A. G., Holtzman, N. M., Rao, K., Xu, L., and Saatchi, S. S.: Interannual Variations of Vegetation Optical Depth are Due to Both Water Stress and Biomass Changes, Geophys. Res. Lett., 48, e2021GL095267, https://doi.org/10.1029/2021GL095267, 2021.

Kumar, L. and Mutanga, O.: Remote Sensing of Above-Ground Biomass, Remote Sens., 9, https://doi.org/10.1029/2018EF00089010.3390/rs9090935, 2017.

Le Toan, T., Quegan, S., Davidson, M. W. J., Balzter, H., Paillou, P., Papathanassiou, K., Plummer, S., Rocca, F., Saatchi, S., Shugart, H., and Ulander, L.: The BIOMASS mission: Mapping global forest biomass to better understand the terrestrial carbon cycle, Remote. Sens. Environ., 115, 2850-2860, https://doi.org/10.1016/j.rse.2011.03.020, 2011.

Leys, C., Ley, C., Klein, O., Bernard, P., and Licata, L.: Detecting outliers: Do not use standard deviation around the mean, use absolute deviation around the median, J. Exp. Soc. Psychol., 49, 764-766, https://doi.org/10.1016/j.jesp.2013.03.013, 2013.

Li, W., MacBean, N., Ciais, P., Defourny, P., Lamarche, C., Bontemps, S., Houghton, R. A., and Peng, S.: Gross and net land cover changes in the main plant functional types derived from the annual ESA CCI land cover maps (1992–2015), Earth Syst.

Sci. Data, 10, 219-234, https://doi.org/10.1029/2018EF00089010.5194/essd-10-219-2018, 2018.

Li, X., Wigneron, J.-P., Frappart, F., Fan, L., Ciais, P., Fensholt, R., Entekhabi, D., Brandt, M., Konings, A. G., Liu, X., Wang, M., Al-Yaari, A., and Moisy, C.: Global-scale assessment and inter-comparison of recently developed/reprocessed microwave satellite vegetation optical depth products, Remote. Sens. Environ., 253, 112208, https://doi.org/10.1016/j.rse.2020.112208, 2021.

Liu, M., Li, D., Hu, J., Liu, D., Ma, Z., Cheng, X., Zhao, C., and Liu, Q.: Altitudinal pattern of shrub biomass allocation in Southwest China, PLoS One, 15, e0240861, https://doi.org/10.1029/2018EF00089010.1371/journal.pone.0240861, 2020.

Liu, X., Su, Y., Hu, T., Yang, Q., Liu, B., Deng, Y., Tang, H., Tang, Z., Fang, J., and Guo, Q.: Neural network guided interpolation for mapping canopy height of China's forests by integrating GEDI and ICESat-2 data, Remote. Sens. Environ., 269, 112844, https://doi.org/10.1016/j.rse.2021.112844, 2022.

Liu, Y. Y., de Jeu, R. A. M., McCabe, M. F., Evans, J. P., and van Dijk, A. I. J. M.: Global long-term passive microwave satellite-based retrievals of vegetation optical depth, Geophys. Res. Lett., 38, https://doi.org/10.1029/2011GL048684, 2011.

Liu, Y. Y., van Dijk, A. I. J. M., de Jeu, R. A. M., Canadell, J. G., McCabe, M. F., Evans, J. P., and Wang, G.: Recent reversal in loss of global terrestrial biomass, Nat. Clim. Change, 5, 470-474, https://doi.org/10.1029/2018EF00089010.1038/nclimate2581, 2015.

Lu, F., Hu, H., Sun, W., Zhu, J., Liu, G., Zhou, W., Zhang, Q., Shi, P., Liu, X., Wu, X., Zhang, L., Wei, X., Dai, L., Zhang, K., Sun, Y., Xue, S., Zhang, W., Xiong, D., Deng, L., Liu, B., Zhou, L., Zhang, C., Zheng, X., Cao, J., Huang, Y., He, N., Zhou, G., Bai, Y., Xie, Z., Tang, Z., Wu, B., Fang, J., Liu, G., and Yu, G.: Effects of national ecological restoration projects on carbon sequestration in China from 2001 to 2010, P. Natl. Acad. Sci. USA, 115, 4039-4044, https://doi.org/10.1029/2018EF00089010.1073/pnas.1700294115, 2018.

Luo, T.: Patterns of net primary productivity for Chinese major forest types and their mathematical models, Chinese Academy of Sciences, 1996.

Luo, Y., Zhang, X., Wang, X., and Lu, F.: Biomass and its allocation of Chinese forest ecosystems, Ecology, 95, 2026-2026, https://doi.org/10.1890/13-2089.1, 2014.

Luo, Y., Wang, X., Zhang, X., Booth, T. H., and Lu, F.: Root:shoot ratios across China's forests: Forest type and climatic effects, Forest Ecol. Manag., 269, 19-25, https://doi.org/10.1016/j.foreco.2012.01.005, 2012.

Ma, H., Mo, L., Crowther, T. W., Maynard, D. S., van den Hoogen, J., Stocker, B. D., Terrer, C., and Zohner, C. M.: The global distribution and environmental drivers of aboveground versus belowground plant biomass, Nat. Ecol. Evol., https://doi.org/10.1038/s41559-021-01485-1, 2021.

Markus, T., Neumann, T., Martino, A., Abdalati, W., Brunt, K., Csatho, B., Farrell, S., Fricker, H., Gardner, A., Harding, D., Jasinski, M., Kwok, R., Magruder, L., Lubin, D., Luthcke, S., Morison, J., Nelson, R., Neuenschwander, A., Palm, S., Popescu, S., Shum, C. K., Schutz, B. E., Smith, B., Yang, Y., and Zwally, J.: The Ice, Cloud, and land Elevation Satellite-2 (ICESat-2): Science requirements, concept, and implementation, Remote. Sens. Environ., 190, 260-273, https://doi.org/10.1016/j.rse.2016.12.029, 2017.

Menenti, M., Azzali, S., Verhoef, W., and van Swol, R.: Mapping agroecological zones and time lag in vegetation growth by

means of fourier analysis of time series of NDVI images, Adv. Space Res., 13, 233-237, https://doi.org/10.1016/0273-1177(93)90550-U, 1993.

Mialon, A., Rodríguez-Fernández, N. J., Santoro, M., Saatchi, S., Mermoz, S., Bousquet, E., and Kerr, Y. H.: Evaluation of the Sensitivity of SMOS L-VOD to Forest Above-Ground Biomass at Global Scale, Remote Sens., 12, 1450, https://doi.org/10.3390/rs12091450, 2020.

Moesinger, L., Dorigo, W., de Jeu, R., van der Schalie, R., Scanlon, T., Teubner, I., and Forkel, M.: The global long-term microwave Vegetation Optical Depth Climate Archive (VODCA), Earth Syst. Sci. Data, 12, 177-196, https://doi.org/10.5194/essd-12-177-2020, 2020.

Mokany, K., Raison, R. J., and Prokushkin, A. S.: Critical analysis of root: shoot ratios in terrestrial biomes, Global Change Biol., 12, 84-96, https://doi.org/10.1111/j.1365-2486.2005.001043.x, 2006.

Neuenschwander, A., Guenther, E., White, J. C., Duncanson, L., and Montesano, P.: Validation of ICESat-2 terrain and canopy heights in boreal forests, Remote. Sens. Environ., 251, 112110, https://doi.org/10.1016/j.rse.2020.112110, 2020.

Nie, X., Yang, Y., Yang, L., and Zhou, G.: Above- and Belowground Biomass Allocation in Shrub Biomes across the Northeast Tibetan Plateau, PLoS One, 11, e0154251, https://doi.org/10.1371/journal.pone.0154251, 2016.

Niu, Q., Xiao, X., Zhang, Y., Qin, Y., Dang, X., Wang, J., Zou, Z., Doughty, R. B., Brandt, M., Tong, X., Horion, S., Fensholt, R., Chen, C., Myneni, R. B., Xu, W., Di, G., and Zhou, X.: Ecological engineering projects increased vegetation cover, production, and biomass in semiarid and subhumid Northern China, Land Degrad. Dev., 30, 1620-1631, https://doi.org/10.1002/ldr.3351, 2019.

O'Neill, P. E., Chan, S., Njoku, E. G., Jackson, T., Bindlish, R., and Chaubell, J.: SMAP Enhanced L3 Radiometer Global Daily 9 km EASE-Grid Soil Moisture, Version 5., NASA National Snow and Ice Data Center Distributed Active Archive Center. [dataset], https://doi.org/10.5067/4DQ54OUIJ9DL., 2021.

Peng, S., Wen, D., He, N., Yu, G., Ma, A., and Wang, Q.: Carbon storage in China's forest ecosystems: estimation by different integrative methods, Ecol. Evol., 6, 3129-3145, https://doi.org/10.1002/ece3.2114, 2016.

Ploton, P., Mortier, F., Réjou-Méchain, M., Barbier, N., Picard, N., Rossi, V., Dormann, C., Cornu, G., Viennois, G., Bayol, N., Lyapustin, A., Gourlet-Fleury, S., and Pélissier, R.: Spatial validation reveals poor predictive performance of large-scale ecological mapping models, Nat. Commun., 11, 4540, https://doi.org/10.1038/s41467-020-18321-y, 2020.

Potapov, P., Hansen, M. C., Kommareddy, I., Kommareddy, A., Turubanova, S., Pickens, A., Adusei, B., Tyukavina, A., and Ying, Q.: Landsat Analysis Ready Data for Global Land Cover and Land Cover Change Mapping, Remote Sens., 12, https://doi.org/10.3390/rs12030426, 2020.

Qi, Y., Wei, W., Chen, C., and Chen, L.: Plant root-shoot biomass allocation over diverse biomes: A global synthesis, Glob Ecol. Conserv., 18, e00606, https://doi.org/10.1016/j.gecco.2019.e00606, 2019.

Qiu, Z., Feng, Z., Song, Y., Li, M., and Zhang, P.: Carbon sequestration potential of forest vegetation in China from 2003 to 2050: Predicting forest vegetation growth based on climate and the environment, J. Clean. Prod., 252, 119715, https://doi.org/10.1016/j.jclepro.2019.119715, 2020.

Reich, P. B., Luo, Y., Bradford, J. B., Poorter, H., Perry, C. H., and Oleksyn, J.: Temperature drives global patterns in forest

biomass distribution in leaves, stems, and roots, P. Natl. Acad. Sci. USA, 111, 13721, https://doi.org/10.1073/pnas.1216053111, 2014.

Roerink, G. J., Menenti, M., and Verhoef, W.: Reconstructing cloudfree NDVI composites using Fourier analysis of time series, Int. J. Remote Sens., 21, 1911-1917, https://doi.org/10.1080/014311600209814, 2000.

Saatchi, S. S., Harris, N. L., Brown, S., Lefsky, M., Mitchard, E. T. A., Salas, W., Zutta, B. R., Buermann, W., Lewis, S. L., Hagen, S., Petrova, S., White, L., Silman, M., and Morel, A.: Benchmark map of forest carbon stocks in tropical regions across three continents, P. Natl. Acad. Sci. USA, 108, 9899, https://doi.org/10.1073/pnas.1019576108, 2011.

Santoro, M. and Cartus, O.: ESA Biomass Climate Change Initiative (Biomass_cci): Global datasets of forest above-ground biomass for the year 2017, v1. [dataset], https://doi.org/10.5285/bedc59f37c9545c981a839eb552e4084, 2019.

Santoro, M. and Cartus, O.: ESA Biomass Climate Change Initiative (Biomass_cci): Global datasets of forest above-ground biomass for the years 2010, 2017 and 2018, v3 [dataset], https://doi.org/10.5285/5f331c418e9f4935b8eb1b836f8a91b8, 2021.

Santoro, M., Cartus, O., Carvalhais, N., Rozendaal, D. M. A., Avitabile, V., Araza, A., de Bruin, S., Herold, M., Quegan, S., Rodríguez-Veiga, P., Balzter, H., Carreiras, J., Schepaschenko, D., Korets, M., Shimada, M., Itoh, T., Moreno Martínez, Á., Cavlovic, J., Cazzolla Gatti, R., da Conceição Bispo, P., Dewnath, N., Labrière, N., Liang, J., Lindsell, J., Mitchard, E. T. A., Morel, A., Pacheco Pascagaza, A. M., Ryan, C. M., Slik, F., Vaglio Laurin, G., Verbeeck, H., Wijaya, A., and Willcock, S.: The global forest above-ground biomass pool for 2010 estimated from high-resolution satellite observations, Earth Syst. Sci. Data, 13, 3927-3950, https://doi.org/10.5194/essd-13-3927-2021, 2021.

Simard, M., Pinto, N., Fisher, J. B., and Baccini, A.: Mapping forest canopy height globally with spaceborne lidar, J. Geophys. Res.-Biogeo., 116, https://doi.org/10.1029/2011JG001708, 2011.

Spawn, S. A., Sullivan, C. C., Lark, T. J., and Gibbs, H. K.: Harmonized global maps of above and belowground biomass carbon density in the year 2010, Sci. Data, 7, 112, https://doi.org/10.1038/s41597-020-0444-4, 2020.

Stegen, J. C., Swenson, N. G., Enquist, B. J., White, E. P., Phillips, O. L., Jørgensen, P. M., Weiser, M. D., Monteagudo Mendoza, A., and Núñez Vargas, P.: Variation in above-ground forest biomass across broad climatic gradients, Global Ecol. Biogeogr., 20, 744-754, https://doi.org/10.1111/j.1466-8238.2010.00645.x, 2011.

Su, Y., Guo, Q., Xue, B., Hu, T., Alvarez, O., Tao, S., and Fang, J.: Spatial distribution of forest aboveground biomass in China: Estimation through combination of spaceborne lidar, optical imagery, and forest inventory data, Remote. Sens. Environ., 173, 187-199, https://doi.org/10.1016/j.rse.2015.12.002, 2016.

Sun, X., Wang, G., Huang, M., Chang, R., and Ran, F.: Forest biomass carbon stocks and variation in Tibet's carbon-dense forests from 2001 to 2050, Sci. Rep., 6, 34687, https://doi.org/10.1038/srep34687, 2016.

Tang, X., Zhao, X., Bai, Y., Tang, Z., Wang, W., Zhao, Y., Wan, H., Xie, Z., Shi, X., Wu, B., Wang, G., Yan, J., Ma, K., Du, S., Li, S., Han, S., Ma, Y., Hu, H., He, N., Yang, Y., Han, W., He, H., Yu, G., Fang, J., and Zhou, G.: Carbon pools in China's terrestrial ecosystems: New estimates based on an intensive field survey, P. Natl. Acad. Sci. USA, 115, 4021, https://doi.org/10.1073/pnas.1700291115, 2018.

Thurner, M., Beer, C., Santoro, M., Carvalhais, N., Wutzler, T., Schepaschenko, D., Shvidenko, A., Kompter, E., Ahrens, B., Levick, S. R., and Schmullius, C.: Carbon stock and density of northern boreal and temperate forests, Global Ecol. Biogeogr.,

23, 297-310, https://doi.org/10.1111/geb.12125, 2014.

Tong, X., Brandt, M., Yue, Y., Horion, S., Wang, K., Keersmaecker, W. D., Tian, F., Schurgers, G., Xiao, X., Luo, Y., Chen, C., Myneni, R., Shi, Z., Chen, H., and Fensholt, R.: Increased vegetation growth and carbon stock in China karst via ecological engineering, Nat. Sustain., 1, 44-50, https://doi.org/10.1038/s41893-017-0004-x, 2018.

Tong, X., Brandt, M., Yue, Y., Ciais, P., Rudbeck Jepsen, M., Penuelas, J., Wigneron, J.-P., Xiao, X., Song, X.-P., Horion, S., Rasmussen, K., Saatchi, S., Fan, L., Wang, K., Zhang, B., Chen, Z., Wang, Y., Li, X., and Fensholt, R.: Forest management in southern China generates short term extensive carbon sequestration, Nat. Commun., 11, 129, https://doi.org/10.1038/s41467-019-13798-8, 2020.

Verger, A., Baret, F., and Weiss, M.: Near Real-Time Vegetation Monitoring at Global Scale, IEEE J-Stars, 7, 3473-3481, https://doi.org/10.1109/JSTARS.2014.2328632, 2014.

Wang, J., Feng, L., Palmer, P. I., Liu, Y., Fang, S., Bösch, H., O'Dell, C. W., Tang, X., Yang, D., Liu, L., and Xia, C.: Large Chinese land carbon sink estimated from atmospheric carbon dioxide data, Nature, 586, 720-723, https://doi.org/10.1038/s41586-020-2849-9, 2020.

Wang, L., Li, L., Chen, X., Tian, X., Wang, X., and Luo, G.: Biomass Allocation Patterns across China's Terrestrial Biomes, PLoS One, 9, e93566, https://doi.org/10.1371/journal.pone.0093566, 2014.

Wigneron, J.-P., Li, X., Frappart, F., Fan, L., Al-Yaari, A., De Lannoy, G., Liu, X., Wang, M., Le Masson, E., and Moisy, C.: SMOS-IC data record of soil moisture and L-VOD: Historical development, applications and perspectives, Remote. Sens. Environ., 254, 112238, https://doi.org/10.1016/j.rse.2020.112238, 2021.

Xu, B., Guo, Z., Piao, S., and Fang, J.: Biomass carbon stocks in China's forests between 2000 and 2050: A prediction based on forest biomass-age relationships, Science China Life Sciences, 53, 776-783, https://doi.org/10.1007/s11427-010-4030-4, 2010.

Xu, L., Yu, G., He, N., Wang, Q., Gao, Y., Wen, D., Li, S., Niu, S., and Ge, J.: Carbon storage in China's terrestrial ecosystems: A synthesis, Sci. Rep., 8, 2806, https://doi.org/10.1038/s41598-018-20764-9, 2018.

Xu, L., Saatchi, S. S., Yang, Y., Yu, Y., Pongratz, J., Bloom, A. A., Bowman, K., Worden, J., Liu, J., Yin, Y., Domke, G., McRoberts, R. E., Woodall, C., Nabuurs, G.-J., de-Miguel, S., Keller, M., Harris, N., Maxwell, S., and Schimel, D.: Changes in global terrestrial live biomass over the 21st century, Sci. Adv., 7, eabe9829, https://doi.org/10.1126/sciadv.abe9829, 2021.

Yang, D., Liu, Y., Feng, L., Wang, J., Yao, L., Cai, Z., Zhu, S., Lu, N., and Lyu, D.: The First Global Carbon Dioxide Flux Map Derived from TanSat Measurements, Ad. Atmos. Sci., 38, 1433-1443, https://doi.org/10.1007/s00376-021-1179-7, 2021.

Yang, X., Guo, Y., Mohhamot, A., Liu, H., Ma, W., Yu, S., and Tang, Z.: Distribution of biomass in relation to environments in shrublands of temperate China, Chinese Journal of Plant Ecology, 41, 22-30, https://doi.org/10.17521/cjpe.2016.0199, 2017.

Yao, Y., Piao, S., and Wang, T.: Future biomass carbon sequestration capacity of Chinese forests, Sci. Bull., 63, 1108-1117, https://doi.org/10.1016/j.scib.2018.07.015, 2018.

Yin, G., Zhang, Y., Sun, Y., Wang, T., Zeng, Z., and Piao, S.: MODIS Based Estimation of Forest Aboveground Biomass in China, PLoS One, 10, e0130143, https://doi.org/10.1371/journal.pone.0130143, 2015.

https://doi.org/10.5194/essd-2022-286
Preprint. Discussion started: 26 September 2022

745 Zhang, R., Zhou, X., Ouyang, Z., Avitabile, V., Qi, J., Chen, J., and Giannico, V.: Estimating aboveground biomass in subtropical forests of China by integrating multisource remote sensing and ground data, Remote. Sens. Environ., 232, 111341, https://doi.org/10.1016/j.rse.2019.111341, 2019.

Zhang, Y. and Liang, S.: Fusion of Multiple Gridded Biomass Datasets for Generating a Global Forest Aboveground Biomass Map, Remote Sens., 12, https://doi.org/10.3390/rs12162559, 2020.

750 Zhang, Y., Yao, Y., Wang, X., Liu, Y., and Piao, S.: Mapping spatial distribution of forest age in China, Earth Space Sci., 4, 108-116, https://doi.org/10.1002/2016EA000177, 2017.